INTERNATIONAL JOURNAL FOR NUMERICAL METHODS IN FLUIDS
Int. J. Numer. Meth. Fluids 2010; **00**:1–19
Published online in Wiley InterScience (www.interscience.wiley.com). DOI: 10.1002/fld

An Efficient WENO Limiter for Discontinuous Galerkin Transport Scheme on the Cubed Sphere

Wei Guo[1], Ramachandran D. Nair [2]and Xinghui Zhong[1]*

[1]*Department of Mathematics, Michigan State University, East Lansing, MI 48824*
[2]*National Center for Atmospheric Research, Boulder, CO 80305*

SUMMARY

The discontinuous Galerkin (DG) transport scheme is becoming increasingly popular in the atmospheric modeling due to its distinguished features, such as high-order accuracy and high-parallel efficiency. Despite the great advantages, DG schemes may produce unphysical oscillations in approximating transport equations with discontinuous solution structures including strong shocks or sharp gradients. Nonlinear limiters need to be applied to suppress the undesirable oscillations and enhance the numerical stability. It is usually very difficult to design limiters to achieve both high-order accuracy and non-oscillatory properties, and even more challenging for the cubed-sphere geometry. In this paper, a simple and efficient limiter based on the Weighted Essentially Non-Oscillatory (WENO) methodology is incorporated in the DG transport framework on the cubed sphere. The uniform high-order accuracy of the resulting scheme is maintained due to the high-order nature of WENO procedures. Unlike the classic WENO limiter, for which the wide halo region may significantly impede parallel efficiency, the simple limiter requires only the information from the nearest neighboring elements without degrading the inherent high-parallel efficiency of the DG scheme. A bound-preserving filter can be further coupled in the scheme which guarantees the highly desirable positivity-preserving property for the numerical solution. The resulting scheme is high-order accurate, non-oscillatory, and positivity-preserving for solving transport equations based on the cubed-sphere geometry. Extensive numerical results for several benchmark spherical transport problems are provided to demonstrate good results, both in accuracy and in non-oscillatory performance. Copyright © 2010 John Wiley & Sons, Ltd.

Received ...

KEY WORDS: Discontinuous Galerkin methods; Transport equations; Simple WENO limiter; Bound-preserving filter; Cubed sphere.

1. INTRODUCTION

Discontinuous Galerkin (DG) methods, first introduced in [28], is a class of finite element method with completely discontinuous piecewise polynomials as basis functions. A major development of DG methods was carried out by Cockburn and Shu [4, 5]. They combined the DG spatial discretization method with Runge-Kutta time discretization, known as Runge-Kutta discontinuous Galerkin (RKDG) methods for conservation laws. This methods has several advantages such as geometric flexibility, local conservation, the capability of h-p adaptivity and excellent parallel efficiency. Due to these desirable properties, DG methods are becoming more and more popular in atmosphere modeling [21, 22, 2, 11] on a variety of spherical meshes [8, 12]. We refer the readers to the review paper [23] for details of the various DG applications in atmospheric science with an extensive list of references.

*Correspondence to: Department of Mathematics, Michigan State University, East Lansing, MI 48824. Email: zhongxh@math.msu.edu

Despite the great advantages, DG schemes may fail in approximating transport equations with discontinuous solution structures including strong shocks or sharp gradients. A nonlinear limiter need to be applied to control oscillations near shocks and other discontinuities. It is usually very difficult to design limiters to achieve both high-order accuracy and non-oscillatory properties. Such an attempt has been made in [26, 27, 19], where the WENO methodology and Hermite WENO (HWENO) methodology reconstruction serves as a limiter for RKDG methods. A major drawback of these limiters is that they need wide stencils, which made them hard to implement for multi-dimensional problems and potentially impede the parallel efficiency [18]. More recently, a particularly simple and compact WENO limiter, which utilizes fully the advantage of DG solutions, is designed for RKDG methods in [36, 37]. The idea of this simple limiter is to reconstruct a new polynomial on the target cell which is a convex combination of polynomials on this cell and its immediate neighboring cells, with necessary adjustments to keep the original cell average on the target cell. The nonlinear weights in the convex combination coefficients follows the classical WENO procedure. The main advantage of this limiter is its simplicity in implementation, especially for multi-dimensional meshes.

Efficient tracer transport schemes with monotonic or positivity-preserving properties are extremely important for climate models. For a practical climate model, hundreds of tracers (chemical species) need to be transported for a very long duration of time to study the evolution of these tracers in the atmosphere. In order to remove spurious oscillations in the numerical solution and make the solution physically recognizable, a limiter is usually combined with the transport algorithm. For atmospheric models based on high-order methods such as DG [22] or spectral-element methods [6], the tracer transport is very challenging because of unavailability of efficient limiters. In this paper, an efficient WENO limiter is developed for the DG transport scheme on the cubed sphere, based on the idea of a simple WENO limiter for Cartesian meshes [36]. Similar to Cartesian cases, the DG schemes on the cubed sphere may exhibit unphysical oscillations when the smoothness of tracers is lacking, which could impair the performance of DG schemes to some extent. In order to address the issue, the simple WENO limiter is coupled with the DG transport schemes on the cubed sphere. A special treatment at the cube edges is proposed in order to retain the high-order accuracy of the WENO limiter. On the other hand, preserving the positivity (monotonicity) of the solution is highly desirable for atmospheric transport modeling. While WENO-type limiters can effectively remove spurious oscillations, there is no guarantee that they will always keep the numerical solution within the physical bounds. Further coupling a genuinely high-order bound-preserving (BP) filter developed in [34] can ensure the positivity-preservation properties for DG transport schemes.

The paper is organized as follows. In Section 2, we review the DG transport schemes and the simple WENO limiter on the two-dimensional Cartesian meshes. In Section 3, we extend the simple WENO limiter to the cubed-sphere geometry. Details of the special treatment on the edges are also provided. Numerical examples for a class of benchmark tests are presented in Section 4. Conclusions and future work are given in Section 5.

2. A SIMPLE WENO LIMITER FOR DG METHODS

2.1. DG scheme

Consider the two-dimensional conservative transport equation

$$\begin{aligned} \frac{\partial U}{\partial t} + \nabla \cdot \boldsymbol{F}(u) = 0, \quad \text{in } \mathcal{D} \times [0, T] \\ U(x, y, 0) = U_0(x, y), \end{aligned} \tag{2.1}$$

where $U = U(x, y, t)$ is a conservative quantity, $\boldsymbol{F}$ is the flux function and $\nabla \cdot$ is the divergence operator defined on the domain $\mathcal{D}$.

To apply DG methods for spatial discretizations, we first partition the domain $\mathcal{D}$ into non-overlapping elements (cells) I_{ij} and we assume the cell to be rectangular such that $I_{ij} =$

DOI: 10.1002/fld

$[x_{i-1/2}, x_{i+1/2}] \times [y_{j-1/2}, y_{j+1/2}]$. Denote the center of a cell I_{ij} by (x_i, y_j) where $(x_i = (x_{i+1/2} - x_{i-1/2})/2$ and $y_j = (y_{j+1/2} + y_{j-1/2})/2$, and $\Delta x_i = x_{i+1/2} - x_{i-1/2}$ and $\Delta y_j = y_{j+1/2} - y_{j-1/2}$ as the local mesh sizes. The DG method has its solution as well as the test function space given by $V_h^k = \{v(x) : v(x)|_{I_{ij}} \in P^k(I_{ij})\}$, where $P^k(I_{ij})$ denotes the set of polynomials of degree at most k defined on I_{ij}. A semi-discrete DG method for solving (2.1) is defined as follows: seek an approximate solution $U_h \in V_h^k$, such that for all the test function $\phi_h \in V_h^k$, and for each element I_{ij}, we have

$$\int_{I_{ij}} \frac{\partial U_h}{\partial t} \phi_h dx\, dy = \int_{I_{ij}} \boldsymbol{F}(U_h) \cdot \nabla \phi_h dx\, dy - \int_{\partial I_{ij}} \phi_h \widehat{\boldsymbol{F}(U_h) \cdot \boldsymbol{n}}\, ds, \tag{2.2}$$

where ∂I_{ij} is the boundary corresponding to the cell I_{ij} and $\boldsymbol{n}$ is the outward normal vector. Here $\widehat{\boldsymbol{F}(U_h) \cdot \boldsymbol{n}}$ is the numerical flux or approximate Riemann solver which resolves the discontinuity issue at the cell boundary.

When implementing the the DG scheme (2.2), we first define two independent variables (ξ, η) over the reference element $[-1, 1] \times [-1, 1]$ via the following affine mapping

$$\xi = \frac{2(x - x_i)}{\Delta x_i}, \quad \eta = \frac{2(y - y_j)}{\Delta y_j}; \quad x \times y \in [x_{i-\frac{1}{2}}, x_{i+\frac{1}{2}}] \times [y_{j-\frac{1}{2}}, y_{j+\frac{1}{2}}]. \tag{2.3}$$

Spatial discretization is performed by approximating each function as a sum of polynomial basis functions $\ell(\xi)$, which are the Lagrangian interpolating (orthogonal) polynomials based on the Gaussian-Lobatto-Legendre (GLL) points, given by

$$\ell_m(\xi) = \frac{(\xi - 1)(\xi + 1)\, L_k'(\xi)}{k(k+1)\, L_k(\xi_m)\, (\xi - \xi_m)}, \tag{2.4}$$

where ξ_m, $m = 0, \cdots, k$ are the GLL points over $[-1, 1]$, and $L_k(\xi)$ is the Legendre polynomial of degree k. Two-dimensional basis functions are constructed from a tensor product of the one-dimensional basis, such that the DG solution on a cell I_{ij} can be represented by

$$U_h(x, y, t)|_{I_{ij}} = U_h(\xi, \eta, t)|_{I_{ij}} = \sum_{s=0}^{k} \sum_{m=0}^{k} U_{ij}^{s,m}(t) \ell_s(\xi) \ell_m(\eta), \tag{2.5}$$

where the degree of freedom $U_{ij}^{l,m}(t)$ is the point value of solution U_h at a GLL point (ξ_l, η_m), defined in (2.3) on the cell I_{ij}. Substituting the discretized scalar field (2.5) and test functions into (2.2), and replacing integrals by the Gaussian-Lobatto quadratures converts the partial differential equation into a set of ordinary differential equations (ODEs) in time, which may be written abstractly as

$$\frac{d}{dt} U = \mathcal{L}(U), \tag{2.6}$$

where $\mathcal{L}$ is the spatial discretization operator. To discretize the temporal variable, we use the following strong stability preserving (SSP) third order Runge-Kutta (RK) method [32]:

$$\begin{aligned} U^{(1)} &= U^n + \Delta t \mathcal{L}(u^n), \\ U^{(2)} &= \frac{3}{4} U^n + \frac{1}{4} U^{(1)} + \frac{1}{4} \Delta t \mathcal{L}(U^{(1)}), \\ U^{n+1} &= \frac{1}{3} U^n + \frac{2}{3} U^{(2)} + \frac{2}{3} \Delta t \mathcal{L}(U^{(2)}). \end{aligned} \tag{2.7}$$

Other SSP time discretizations [9] can also be used.

DOI: 10.1002/fld

2.2. *The simple WENO limiter*

To control the oscillations near a shock or other discontinuities in the DG solution, we employ a simple WENO limiting strategy. Such a simple WENO limiter for DG methods was first introduced by [36]. The major difference between this simple WENO limiter and previous WENO and HWENO limiters [27, 24, 35], is that the former one uses a more compact stencil and much easier to implement. Once a cell is identified as an oscillatory (troubled) cell by the Total Variation Bounded (TVB) limiter [4, 5], then we want to replace the solution polynomial on the troubled cell with a reconstructed polynomial. Note that there exist many troubled cell indicators in the literature and readers are referred to [25] a detailed comparison of a variety of troubled cell indicators for DG methods. Generally, there are several requirements for the reconstructed polynomial. First, it should maintain the cell average for conservation. Second, high order accuracy of the original polynomial should be maintained. At last, the new polynomial should be free from oscillations.We briefly outline the procedure below and we refer readers to [36] for more details.

The first step is to preprocess the polynomials U_n from the neighboring cells, for which a reconstruction stencil is required. Each stencil consists of a target (or "troubled") cell I_0 and its four nearest neighbors which share the edge with the target cell, as depicted schematically in Figure 2.1(a). This step is to modify the polynomials on the neighboring cells by an addition of a constant to keep the original cell average of the DG solution on the target cell. The simple WENO limiter is to reconstruct a new polynomial on the target cell which is a convex combination of polynomial on the cell itself and preprocessed polynomials on its immediate neighboring cells. The nonlinear weights ω_n of the convex combination depends on the local smoothness of the solution polynomial, and thus creates the non-oscillatory solution. The smoothness indicators β_n are a measure of the smoothness of the polynomial U_n. The smoother the polynomial U_n is, the smaller value of the smoothness indicator β_n is. The smoothness indicators are then used to convert the preselected linear weights (γ_n) to nonlinear weights (ω_n).

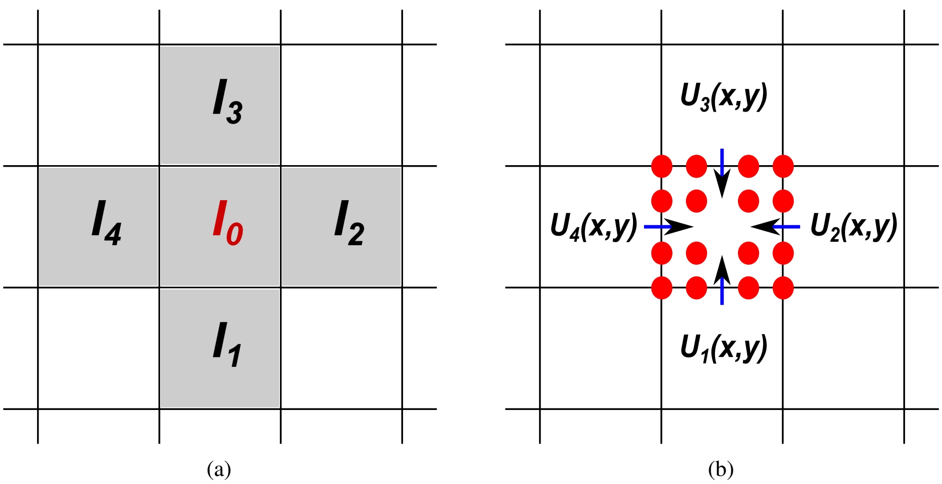

Figure 2.1. (a): The stencil used for the simple WENO reconstruction on a target cell I_{ij} are shown for a single index I_0; the shaded 5 cells comprise the reconstruction stencil. (b): Extrapolation (extension) procedure in order to reconstruct a new polynomial

The major difference between the simple WENO limiter and previous WENO or HWENO limiters is that the former uses most fully the information of the complete polynomials which are already available for DG methods in the target and neighboring cells, while the latter need to reconstruct the point values or moments individually and separately. The simple WENO limiter approach simultaneously removes the problem of negative weights and reduces considerably the complexity of implementation. Moreover, the richness of available information make the choice of

DOI: 10.1002/fld

linear weights much less restrictive and the simple WENO limiter scheme more easy to implement and computationally attractive.

To better illustrate the reconstruction procedure of the simple WENO limiter, we start with the assumption that the cell I_{ij} is identified as a troubled cell by the TVB troubled cell indicator [4, 5]. The reconstruction employs a stencil with five cells as shown in Figure 2.1(a), i.e., the target cell located at the center and its four nearest neighbors. For convenience, we denote the cells with a single index I_l, $l = l(i, j)$ and denote the DG solution polynomials on the cells I_l as $U_l(x, y),\ l = 0, 1, \cdots, 4$, where $U_0(x, y)$ is located on the troubled cell I_0. We want to reconstruct a new polynomial $U_0^{new}(x, y)$ on the target cell using the information of the polynomial $U_0(x, y)$ on the troubled cell I_0 and the polynomials $\{U_l(x, y)\}_{l=1}^4$ on its neighboring cells, as indicated in Figure 2.1(a).

Since our goal is to construct a new polynomial on the target cell I_0, for convenience, we now try to represent the four polynomials $\{U_l(x, y)\}_{l=1}^4$ on the neighboring cells using the local basis functions of the target cell I_0. This step can be considered as the extension of the polynomials from the neighboring cells to the target cell, as shown in Figure 2.1(b). It can also be considered as extrapolating the values at the GLL points over the cell I_0 through the polynomials $U_l(x, y)$, $l = 1, \cdots, 4$ on the four neighboring cells, thereby constructing four new polynomials on the target cell I_0 denoted by $U_{0,l}(x, y)$, $l = 1, \cdots, 4$, as shown in Figure 2.1(b). Under the choice of our basis functions and according to (2.5), we can represent $U_{0,l}(x, y)$ via (ξ, η) as

$$U_{0,l}(\xi, \eta) = \sum_{s=0}^{k} \sum_{m=0}^{k} U_{l,0}^{s,m} \ell_s(\xi) \ell_m(\eta), \quad l = 1, \cdots, 4, \tag{2.8}$$

where $U_{l,0}^{s,m}$ is the point value of solution U_l at a GLL point (ξ_s, η_m), defined in (2.3) on the cell I_0, i.e.

$$U_{l,0}^{s,m} = U_l(\xi_s, \eta_m). \tag{2.9}$$

As in [36], in order to make sure that the reconstructed polynomials $U_{0,l}(x, y)$ maintains the original cell average of $U_0(x, y)$ on the target cell I_0, we preprocess the four polynomials $U_{0,l}(x, y)$, $l = 1, \cdots, 4$ and denote the preprocessed polynomial as $\widetilde{U}_l$:

$$\widetilde{U}_{0,l}(x, y) = U_{0,l}(x, y) + C_l, \quad l = 1, \cdots, 4. \tag{2.10}$$

Here C_l is the adjusting constant to maintain the cell average and hence the conservation property, given by

$$C_l = \frac{1}{\Delta x_i \Delta y_j} \int_{I_0} (U_0(x, y) - U_{0,l}(x, y))\, dx\, dy = \frac{1}{4} \sum_{s=0}^{k} \sum_{m=0}^{k} w_s w_m \left(U_0^{s,m} - U_{0,l}^{s,m} \right), \tag{2.11}$$

where w_m, $m = 0, \cdots, k$ are the corresponding Gauss-Lobatto quadrature weights on $[-1, 1]$. Since the moments of $\widetilde{U}_{0,l}(x, y)$, $\widetilde{U}_{0,l}^{s,m}$, is the point value of $\widetilde{U}_{0,l}(x, y)$ at the GLL point $(\xi_s,\ \eta_m)$ on the cell I_0, by (2.10) and (2.8), we have

$$\widetilde{U}_{0,l}^{s,m} = U_{l,0}^{s,m} + C_l \tag{2.12}$$

with $U_{l,0}^{s,m}$ given by (2.9) and C_l given by (2.11).

With the original polynomial $U_0(x, y)$ on the target cell and the preprocessed polynomials $\widetilde{U}_{0,l}(x, y)$, $l = 1, \cdots, 4$ from the four neighboring cells, we now are able to determine the convex combination coefficients follow the classical WENO procedure. First we choose the linear weights and denote as γ_l, $l = 0, 1, \cdots, 4$. Following the practice in [7, 36], we put a larger linear weight on the troubled cell and the neighboring cells get smaller linear weights. For example, in our numerical results, we take

$$\begin{aligned} &\gamma_0 = 0.996, \quad \gamma_1 = \gamma_2 = \gamma_3 = \gamma_4 = 0.001, \quad \text{for} \quad P^2 \quad \text{case}, \\ &\gamma_0 = 0.9996, \quad \gamma_1 = \gamma_2 = \gamma_3 = \gamma_4 = 0.0001, \quad \text{for} \quad P^3 \quad \text{case}. \end{aligned} \tag{2.13}$$

DOI: 10.1002/fld

Next, we compute the smoothness indicators β_l as follows:

$$\beta_l = \sum_{|\alpha|=1}^{k} |I_0|^{|\alpha|-1} \int_{I_0} \left(\frac{\partial^{|\alpha|}}{\partial x^{\alpha_1} \partial y^{\alpha_2}} \widetilde{U}_{0,l}(x,y) \right)^2 dx\, dy, \tag{2.14}$$

where $\alpha = (\alpha_1, \alpha_2)$ and $|I_0| = \Delta x_i \Delta y_j$. For more details about this smoothness indicator, we refer to [14, 1, 31]. Following [14, 13, 1, 15], the normalized nonlinear weights are converted from the linear weights using the smooth indicator as follows:

$$\omega_l = \frac{\bar{\omega}_l}{\sum_s \bar{w}_s}, \quad \bar{\omega}_l = \frac{\gamma_l}{(\varepsilon + \beta_l)^2}, \quad l = 0, 1, \cdots, 4 \tag{2.15}$$

where ε is a small number to avoid a zero denominator. The final nonlinear WENO reconstruction polynomial $U_0^{new}(x,y)$ is now given by

$$U_0^{new}(x,y) = \omega_0 U_0(x,y) + \sum_{l=1}^{4} \omega_l \widetilde{U}_{0,l}(x,y), \tag{2.16}$$

or the degrees of freedom under the nodal basis functions are given by

$$[U_0^{s,m}]^{new} = \omega_0 U_0^{s,m} + \sum_{l=1}^{4} \omega_l \widetilde{U}_{l,0}^{s,m}, \tag{2.17}$$

with $s, m = 0, \cdots, k$.

The simple WENO limiter, like other WENO limiters, is only essentially non-oscillatory and it may not eliminate all small oscillations near the physical bounds. Therefore, we need to further implement a bound-preserving (BP) filter for the DG scheme combined with the simple WENO limiter.

2.3. *The BP filter*

As did in [35], to preserve the initial bounds of the numerical solutions and climate negative densities when positivity is a requirement , we further couple a high-order BP filter [34] into DG transport schemes. The BP filter has several distinctive features. For instance, it is known to be conservative, computationally cheap, and very easy to implement.

Let p_{ij} be the DG solution polynomial on the cell I_{ij} with cell average $\bar{p}_{ij}$. The essential idea of the BP filter is to replace $p_{ij}(x,y)$ with a modified polynomial $\tilde{p}_{ij}(x,y)$ defined as follows

$$\tilde{p}_{ij}(x,y) = \hat{\theta} p_{ij}(x,y) + (1-\hat{\theta})\bar{p}_{ij}, \tag{2.18}$$

$$\hat{\theta} = \min \left\{ \left| \frac{M - \bar{p}_{ij}}{M_{ij} - \bar{p}_{ij}} \right|, \left| \frac{m^\star - \bar{p}_{ij}}{m^\star_{ij} - \bar{p}_{ij}} \right|, 1 \right\} \tag{2.19}$$

where the local extrema are $M_{ij} = \max_{(s,m)} p_{ij}(\xi_s, \eta_m)$ and $m^\star_{ij} = \min_{(s,m)} p_{ij}(\xi_s, \eta_m)$ with (ξ_s, η_m), $s, m = 0, \cdots, k$ being the GLL points on cell I_{ij}. Here M and $m^\star$ are the global extrema of the initial condition, which are usually known in the context of a certain atmospheric tracer transport.

3. A SIMPLE WENO LIMITER FOR DG METHODS ON THE CUBED SPHERE

In this section, we extend the DG schemes coupling the simple WENO limiter (DG + WENO) to the cubed-sphere geometry [30, 29].

DOI: 10.1002/fld

3.1. Cubed-sphere geometry

The cubed-sphere geometry is constructed via a central mapping from a sphere to identical six faces (patches) of a cube [30], as shown in Figure 3.1. Note that, unlike the standard latitude-longitude grid, the cubed-sphere counterpart is free of polar singularities. Instead, a weaker singularity on the internal edges of the cube is generated. There exist several types of cubed-sphere geometry in the literature. In this work, we adopt the cubed-sphere geometry based on the gnomonic (equiangular central) projection [29], which offers a more isotropic spherical grid In such a grid system, the gridlines follow nonorthogonal curvilinear coordinate system (x^1, x^2) such that $x^1, x^2 \in [-\pi/4, \pi/4]$ on each face, as shown in Figure 3.1. Each face of the cubed-sphere is tiled with $N_e \times N_e$ cells so that $6 \times N_e^2$ elements span the entire spherical domain. Below, $N_e \times N_e \times 6$ is used to denote a cubed-sphere mesh.

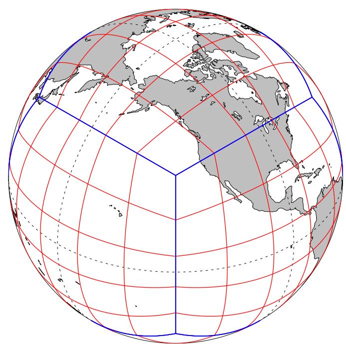

(a)

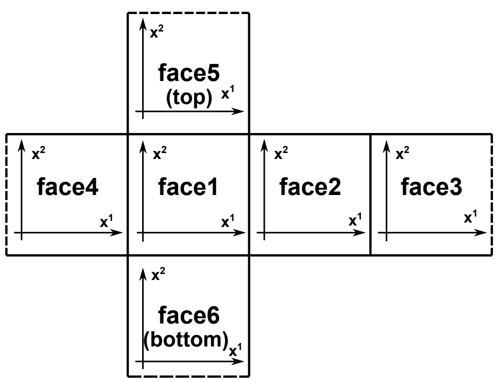

(b)

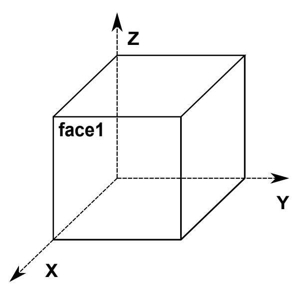

(c)

Figure 3.1. (a): Schematic for the cubed-sphere geometry. (b): The relative positions of six cube faces (from face1 to face6) and their local connectivity.

DOI: 10.1002/fld

Consider the transport equation (2.1), where the computation domain $\mathcal{D}$ is the sphere. In the curvilinear coordinates, the equation can be written as follows

$$\frac{\partial U}{\partial t} + \frac{1}{\sqrt{g}}\frac{\partial}{\partial x^1}(u^1\sqrt{g}\,U) + \frac{1}{\sqrt{g}}\frac{\partial}{\partial x^2}(u^2\sqrt{g}\,U) = 0, \tag{3.1}$$

where $\sqrt{g}$ is the Jacobian (metric term) of the transformation and (u^1, u^2) is the contravariant velocity vector. Further note that the explicit analytical form of $\sqrt{g}$ is available, and it is time independent. By introducing a new unknown scaler $\phi = \sqrt{g}U$ and fluxes $F_1(\phi) = u^1\phi$, $F_2(\phi) = u^2\phi$, equation (3.1) can be rearranged in the following flux form

$$\frac{\partial \phi}{\partial t} + \frac{\partial}{\partial x^1}(F_1(\phi)) + \frac{\partial}{\partial x^2}(F_2(\phi)) = 0, \tag{3.2}$$

which is identical to the two-dimensional Cartesian cases on each cube face. We refer to [21] for details of the transformations.

3.2. A Simple WENO limiter on the cubed sphere

The cubed-sphere geometry offers a quasi-uniform rectangular grid structure and the transport equation (3.2) on the cubed sphere features the same form as the Cartesian cases. Therefore, the DG scheme (2.2) can be conveniently extended to the cubed-sphere case, see [21] for more details. However, as we mentioned above, DG solutions may exhibit non-physical oscillations when approximating non-smooth problems, and hence non-linear limiters are needed to suppress such undesirable oscillations. The situation is similar for the cubed-sphere case, and the inherent complexity of the geometry imposes extra challenges to design satisfactory limiting strategies. Some numerical techniques were developed to address the issue for the DG schemes on the cubed sphere. For example, in [35], a HWENO limiter was developed to attain the non-oscillatory property for the DG P^2 (third-order) schemes. However, we note that there are two concerns about the HWENO limiter. First, the limiter is only third order accurate, which is not sufficient for high order (higher than P^2) DG schemes in order to maintain the same order accuracy. Second, the limiter requires a 3×3 stencil (total 9 cells) for the reconstruction procedure. Note that one cell is ‘missing’ in the stencil for a ‘corner’ element on each cube face; and in such cases, some additional tricks are needed to recover the full 3×3 stencil. To this end, we consider extending the simple WENO limiter for DG on the cubed sphere, which can effectively circumvent the shortcomings: the simple WENO limiter can be designed to be arbitrary high-order accurate with a very compact stencil (5 cells), as shown in Figure 2.1(a). An attractive feature of the simple WENO limiter is that it avoids ghost cells when applied to a corner cell of the cubed sphere, which makes convenient implementation. Moreover, for atmospheric tracer transport problems, preserving the positivity (monotonicity) of the solution is highly desirable [20].

Below, we illustrate the process of coupling the simple WENO limiter reviewed in Section 2.2 into the DG transport on the cubed sphere. Although the DG transport scheme developed for the 2-D Cartesian geometry can be easily implemented on the interior faces, a special attention is required at the edges and corners of the cubed sphere when applying the simple WENO limiter. Due to the coordinate discontinuity at the edges of the cubed-sphere faces, some special treatments are required to guarantee the high order accuracy. For illustrative purposes, we assume that the corner element on face 2, denoted by I_0 ($I_{1,N_e,2}$, where the subindex ‘2’ means the cell locates on face 2), is identified as a troubled cell and the DG solution should be replaced by a reconstructed polynomial, see Figure 3.2(a). The shaded cells constitute a reconstruction stencil, where the single index is also employed for simplicity. In order to obtain the reconstructed polynomial, we need point values at the GLL points over the target cell I_0 from its four neighboring cells via extrapolation. The difficulty lies in the extrapolation process from cell I_3 and cell I_4, where the curvilinear coordinates (x^1, x^2) are discontinuous across the cube edges. However, the issue can be addressed by the following procedure.

For convenience, we denote the GLL points in terms of the local coordinates $(x^1_{\mu,p}, x^2_{\mu,p})$, where $p = 1, \cdots, 6$ indicating the panel index. Here $\mu = (s, m)$ is a single index, $s, m = 0, \cdots, k$, denoting

DOI: 10.1002/fld

the GLL points on each cell. Now, for example, we want to perform the extrapolation procedure from cell I_4 in a high order manner. For each GLL point over the target cell I_0 with the coordinate $(x^1_{\mu,2}, x^2_{\mu,2})$ and the Jacobian $(\sqrt{g})_{\mu,2}$, there is another set of coordinates $(x^1_{\mu,1}, x^2_{\mu,1})$ and the corresponding Jacobian $(\sqrt{g})_{\mu,1}$ given by the central projection transformation on face-1, which is beyond the usual range $[-\pi/4, \pi/4]$. Then we can extrapolate the point value at each GLL point on cell I_0, denoted by $\phi^{\mu,1}_{0,4}$ with the coordinates $(x^1_{\mu,1}, x^2_{\mu,1})$ from the polynomial $\phi_4(x^1, x^2)$ on cell I_4, see Figure 3.2(b). By exploiting the following identity

$$U(\lambda, \theta) = \frac{\phi(x^1_1, x^2_1)}{\sqrt{g}(x^1_1, x^2_1)} = \frac{\phi(x^1_2, x^2_2)}{\sqrt{g}(x^1_2, x^2_2)}, \tag{3.3}$$

where (x^1_1, x^2_1) and (x^1_2, x^2_2) are the local coordinates associated with the same physical point with a spherical coordinate (λ, θ), but from the local transformations on face-1 and face-2, respectively, we are able to compute the point value at each GLL point $(x^1_{\mu,2}, x^2_{\mu,2})$ on face-2, denoted by $\phi^{\mu,2}_{0,4}$, as follows

$$\phi^{\mu,2}_{0,4} = \frac{(\sqrt{g})_{\mu,2}}{(\sqrt{g})_{\mu,1}} \phi^{\mu,1}_{0,4}. \tag{3.4}$$

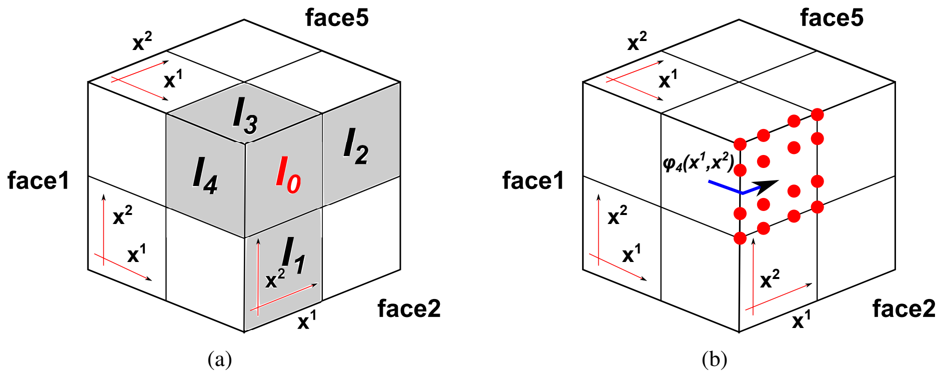

Figure 3.2. (a): The stencil used for the simple WENO reconstruction on a corner cell I_0 is shown for a single index. (b): Extrapolation (extension) procedure from the polynomial $\phi_4(x^1, x^2)$ on the neighboring cell I_4.

Following the similar way, the extrapolating point values at GLL points from cell I_3, denoted by $\phi^{\mu,2}_{0,3}$, can also be obtained. Consequently, we can construct four candidate polynomials $\phi_{0,l}(x^1, x^2)$, $l = 1, \cdots, 4$ from four neighbors. After adjusting the cell average of each polynomial as done in (2.10) and (2.11), the classic WENO procedure is applied to reconstruct a new polynomial $\phi^{new}_0(x^1, x^2)$ as the two-dimensional Cartesian case discussed in Section 2. We remark that the proposed strategy is high-order accurate, since the transformation on each individual face is smooth and the extrapolation process is done in a high-order way.

4. NUMERICAL RESULTS

In this section, we apply the proposed scheme to several benchmark transport problems on the sphere, including the solid-body rotation [33] and the deformational flow [20]. Through these tests, we numerically demonstrate the high-order accuracy, and the non-oscillatory and positivity-preserving properties of the cubed-sphere-based DG transport schemes when coupling the simple WENO limiter and the BP filter. In the simulations, we adopt P^2 (3×3 GLL points per element) and P^3 (4×4 GLL points per element) for the DG discretization, while pointing out that the simple WENO limiter can be combined with any configuration of DG. Note that the P^3 stencil is used the standard configuration for practical model such as [6], with explicit time stepping.

DOI: 10.1002/fld

4.1. Solid-Body Rotation Test Cases

The solid-body rotation is a widely used 2-D spherical advection problem for assessing the quality of a transport scheme. Denote $R = 6.37122 \times 10^6$ m as the earth's radius. The wind components in the longitudinal (λ) and latitudinal (θ) directions are defined as follows:

$$\begin{aligned} u &= u_0(\cos\alpha_0 \cos\theta + \sin\alpha_0 \cos\lambda \sin\theta), \\ v &= -u_0 \sin\alpha_0 \sin\lambda, \end{aligned} \tag{4.1}$$

where $u_0 = 2\pi R/(12 \text{ days})$ meaning that a scaler field U takes 12 simulated days (288 hours(h)) to complete one revolution without any deformation of the shape; α is the rotation angle between the axis of the solid-body rotation and the polar axis of the spherical coordinate. The flow is oriented along the equatorial (east-west) direction when $\alpha = 0$ and the diagonal (north-east) direction when $\alpha = \pi/4$. It is easy to check that the wind field is non-divergent, and hence the maximum principle of solutions holds.

We consider three initial distributions, including a cosine-bell, a Gaussian hill, and a step-cylinder. The cosine-bell initial field is defined by

$$U(\lambda, \theta, t = 0) = \begin{cases} (h_0/2)[1 + \cos(\pi r_d/r_0)] & \text{if} \quad r_d < r_0 \\ 0 & \text{if} \quad r_d \geq r_0, \end{cases} \tag{4.2}$$

where r_d is the great-circle distance between (λ, θ) and the center of the bell which locates at $(3\pi/2, 0)$, $h_0 = 1000$m is the maximum height of the cosine bell, and $r_0 = R/3$ represents its radius. Note that since the exact solution is known at all times, error measures can be computed for checking the accuracy of a spherical transport scheme.

Even though the standard cosine-bell advection test (4.2) provides a good criterion to assess performance of a transport scheme, it can not be used for the convergence study due to the quasi-smoothness (C^1) of the cosine-bell. In order to demonstrate the high-order accuracy of the proposed scheme, we consider using the following smooth (C^∞) Gaussian hill defined by [18],

$$U(\lambda, \theta, t = 0) = h_{max} \exp\left(-b_0 \left((X - X_c)^2 + (Y - Y_c)^2 + (Z - Z_c)^2\right)\right) \tag{4.3}$$

with

$$(X, Y, Z) = (R\cos\theta\cos\lambda, R\cos\theta\sin\lambda, R\sin\theta), \tag{4.4}$$

where $h_{max} = 100$ represents the height of the Gaussian hill and we choose $b_0 = 5$ in the simulation. The center of the Gaussian hill is located at $(\lambda_c, \theta_c) = (3\pi/2, 0)$. The corresponding Cartesian coordinates (X_c, Y_c, Z_c) can be obtained through the relation (4.4).

The last initial field we consider is the step-cylinder defined as follows:

$$U(\lambda, \theta, t = 0) = \begin{cases} h_1 & \text{if} \quad r_d < r_1, \\ h_2 & \text{if} \quad r_1 \leq r_d < r_2, \\ 0 & \text{if} \quad r_d \geq r_2, \end{cases} \tag{4.5}$$

where the heights and radii of the cylinders are set as $h_1 = 1000$m and $h_2 = 500$m, and $r_1 = 2/3R$ and $r_2 = 1/3R$, respectively. At time $t = 0$, the center of the step-cylinder is also located at $(\lambda_c, \theta_c) = (3\pi/2, 0)$. Note that, unlike previous two initial conditions, the distribution of the step-cylinder (4.5) is discontinuous, for which a standard DG scheme may generate oscillatory numerical solutions in the vicinities of discontinuities, as shown in Figures 4.3(a) and 4.3(c). Further note that there is an internal discontinuity at level $U = 500$. Below, by solving this example, we will demonstrate the capacity of the proposed schemes in controlling the internal oscillations.

We first solve the solid-body rotation of the cosine-bell (4.2) with the rotation angle $\alpha = \pi/4$. Note that this configuration is the most challenging case, since the bell passes through four vertices, two edges, and all six cubed faces to complete one full rotation. Set the cubed-sphere mesh as $30 \times 30 \times 6$ which corresponds to $1.5°$ equatorial resolution for P^2 and $1°$ resolution for P^3. The

DOI: 10.1002/fld

time step is chosen as $\Delta t = 720$s and we compute the solution after one revolution ($T = 288$h). The evolution histories of the normalized l_1, l_2 and l_∞ errors defined in [20] are reported in Figure 4.1 for DG P^2 and P^3 with and without using the WENO limiter and the BP filter. It is observed that the magnitude of errors becomes larger after the limiter and filter are applied, especially for the l_∞ error. We notice that such phenomena are also observed for many other limiters in the literature, such as the classic WENO limiter [27], the H-WENO limiter [24, 35], the optimization-based limiter [10].

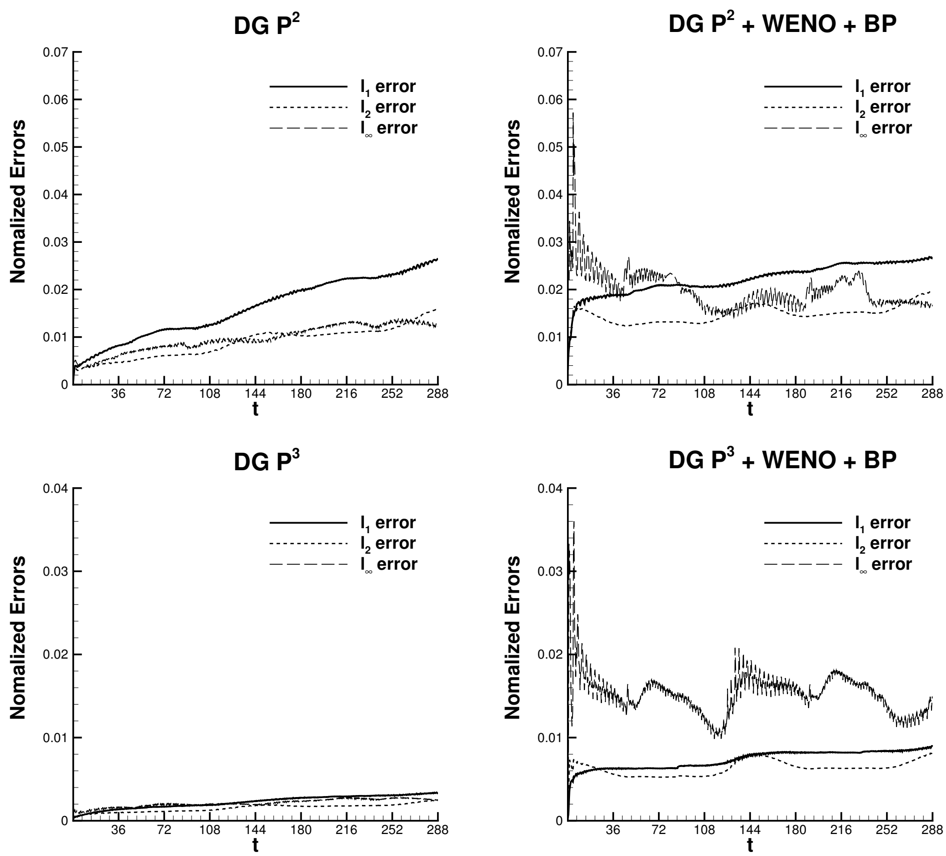

Figure 4.1. The histories of error norms evolution for the solid-body rotation of a cosine-bell. The DG P^2 and P^3 schemes are applied on a cubed-sphere mesh $30 \times 30 \times 6$. The time step is set as Δt = 720 sec and flowangle $\alpha = \pi/4$. (a) Evolution of error norms for the DG P^2 scheme; (b) evolution of error norms for the DG P^2 scheme with the WENO limiter and the BP filter; (c) evolution of error norms for the DG P^3 scheme; (d) evolution of error norms for the DG P^3 scheme with the WENO limiter and the BP filter.

We validate the high-order accuracy of the proposed scheme via the solid-body rotation test with a Gaussian hill initial condition. For this test, the flow is oriented with a rotation angle $\alpha = \pi/4$. Note that, for this smooth problem, the standard DG methods can perfectly resolve the solution structures without producing non-physical oscillations, and hence limiting strategies are not desirable. However, in order to investigate the effect of the WENO limiter on the convergence of DG methods, we choose a very small TVB constant $M = 1E-5$, which results in many 'good' elements are being identified as troubled elements. In Figure 4.2, we report the convergence of the normalized l_1 and l_∞ errors for the DG P^2 (top) and P^3 (bottom) with and without the WENO limiter and the BP filter. It is observed that, even though the WENO limiter is 'artificially' used in many 'good' elements with smooth solutions, the high-order accuracy of DG schemes is still maintained.

DOI: 10.1002/fld

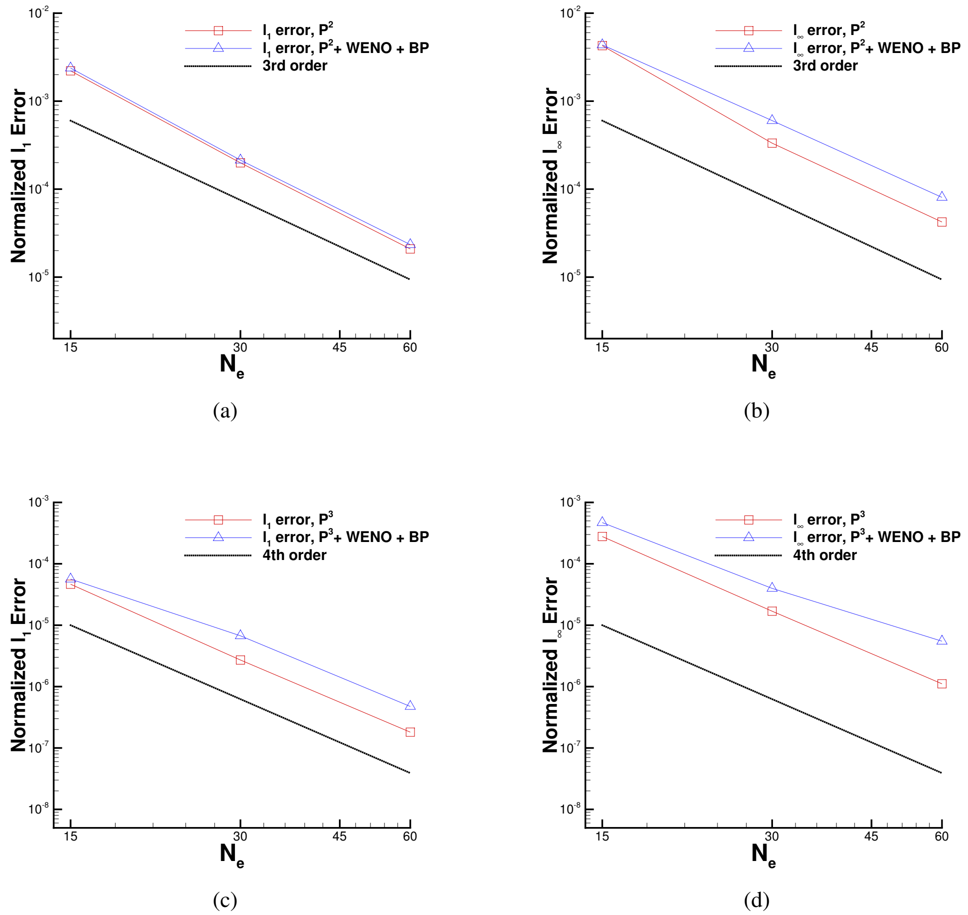

Figure 4.2. Convergence plots of the solid-body rotation of a Gaussian hill. (a) DG P^2; (b) DG P^2 + WENO + BP; (c) DG P^3; (d) DG P^3 + WENO + BP.

Then, we would like to demonstrate the non-oscillatory property of the proposed scheme by using a step-cylinder (4.5) as an initial field. This discontinuous function has three steps with values 0, 500, and 1000 on the sphere. Again, the rotation angle is set as the most challenging one, $\alpha = \pi/4$. We use a $60 \times 60 \times 6$ cubed-sphere mesh and the time step is chosen as $\Delta t = 360$s. The numerical solution is computed up to $T = 288$h. In order to better compare the performance of the schemes, we report the 3-D perspective of the numerical solutions by DG P^2 and DG P^3 projected on the cubed-sphere face-4 in Figure 4.3. As we mentioned, a standard DG scheme may produce oscillatory solutions around discontinuities, as shown in Figures 4.3(a) and 4.3(c). When the simple WENO limiter is applied, such non-physical oscillations are completely removed, as shown in Figures 4.3(b) and 4.3(d). Moreover, the numerical solution is exactly positivity-preserving when further coupling the BP filter. Note that, as pointed out in [35], the BP filter can remove the oscillations near the bound of a DG solution, while it has no control of the internal oscillations. On the other hand, the simple WENO limiter can effectively suppress such internal oscillations, see, e.g., solutions at level 500 in Figure 4.3; and hence the non-oscillatory property is attained when the WENO limiter is coupled into the DG framework.

At last, we study the additional computational overhead required for the simple WENO limiter and the BP filter. For the solid-body rotation test, it is found that the DG scheme coupled with the simple WENO limiter and the BP filter consumes approximately 27% more computational time

Prepared using fldauth.cls
DOI: 10.1002/fld

than the standard DG scheme for both P^2 and P^3 cases. Note that such a combination is more computationally efficient than the DG scheme combined with the H-WENO limiter and the BP filter in [35], which takes about 40% more time.

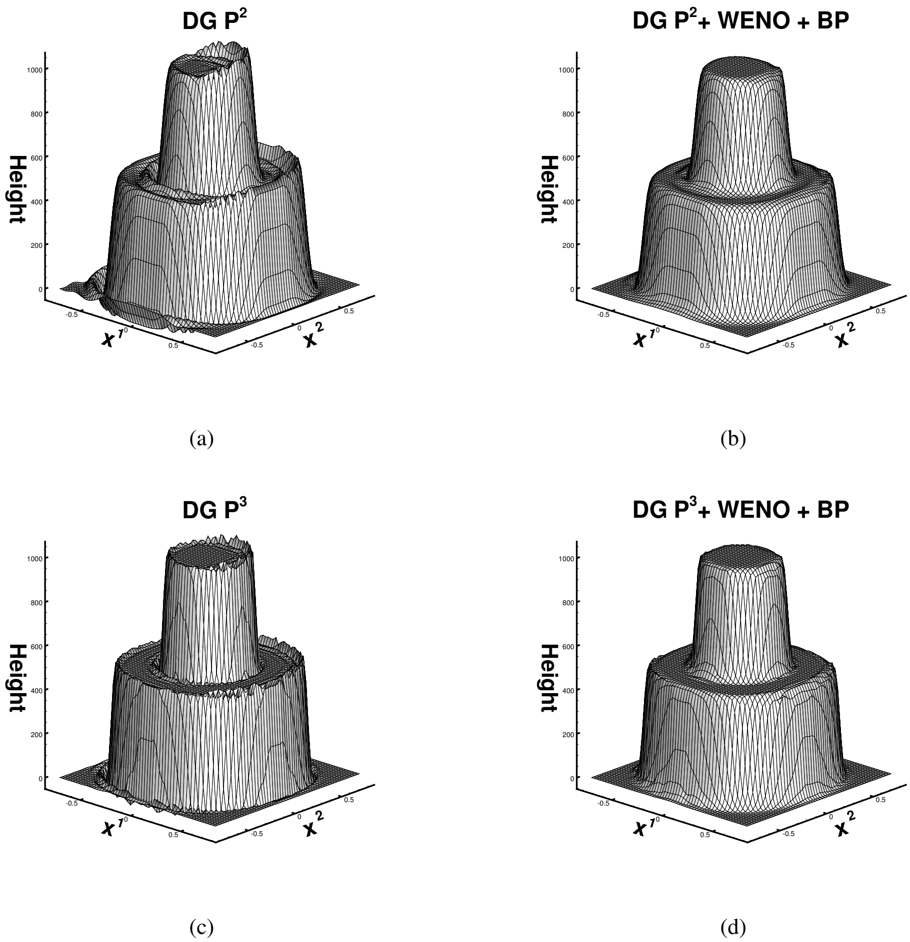

Figure 4.3. 3-D perspective of the numerical solutions projected on the cubed-sphere face-4 for the solid-body rotation of a step-cylinder. The DG P^2 and P^3 schemes are applied on the cubed-sphere meshes $60 \times 60 \times 6$. The flowangle $\alpha = \pi/4$. (a) Numerical solutions by DG P^2; (b) numerical solutions by DG P^2 + WENO + BP; (c) numerical solutions by DG P^3; (d) numerical solutions by DG P^2 + WENO + BP. Numerical oscillations around the discontinuities are clearly observed for the standard DG schemes, see (a) and (c), while such undesirable oscillations are removed by the simple WENO limiter and the BP filter, see (b) and (d).

4.2. *Deformational Flow Test Cases*

To further validate the proposed transport scheme on the sphere, we consider a challenging test from a class of deformational flow tests proposed by [20]. The wind field is defined by

$$
\begin{aligned}
u(\lambda, \theta, t) &= \kappa \sin^2(\lambda') \sin(2\theta) \cos(\pi t/T) + 2\pi \cos(\theta)/T, \\
v(\lambda, \theta, t) &= \kappa \sin(\lambda') \cos(\theta) \cos(\pi t/T),
\end{aligned}
$$

where $\lambda' = \lambda - 2\pi t/T$, $\kappa = 2$ and $T = 5$ units. Note that the wind field is non-divergent and designed to be a combination of a deformational field and a zonal background flow in order to

Int. J. Numer. Meth. Fluids (2010)
DOI: 10.1002/fld

avoid the possible cancellations of errors due to the reversal of the flow along the same flow path after the half time $T/2$.

We also consider three initial conditions to assess the quality of the proposed schemes. The first one is the non-smooth twin slotted-cylinder as an initial condition

$$U^{(sc)}(\lambda,\theta,t=0)=\begin{cases} c & \text{if} \quad r_i \le r \quad \text{and} \quad |\lambda-\lambda_i| \ge r/6 \quad \text{for} \quad i=1,2, \\ c & \text{if} \quad r_1 \le r \quad \text{and} \quad |\lambda-\lambda_1| < r/6 \quad \text{and} \quad \theta-\theta_1 < -\frac{5}{12}r, \\ c & \text{if} \quad r_2 \le r \quad \text{and} \quad |\lambda-\lambda_2| < r/6 \quad \text{and} \quad \theta-\theta_2 > \frac{5}{12}r, \\ b & \text{otherwise} \end{cases} \tag{4.6}$$

where $c=1$, the background value is $b=0.1$, $r=1/2$ is the radius of the cylinders, and $r_i = r_i(\lambda,\theta)$, $i=1,\,2$, is the great-circle distance between (λ,θ) and a specified center (λ_i,θ_i) of one cylinder, which is given by

$$r_i(\lambda,\theta)=\arccos\left(\sin\theta_i\sin\theta+\cos\theta_i\cos\theta\cos(\lambda-\lambda_i)\right), \quad i=1,2.$$

The centers of the twin slotted-cylinder are located at $(\lambda_1,\theta_1)=(5\pi/6,0)$ and $(\lambda_2,\theta_2)=(7\pi/6,0)$, respectively. Figure 4.4(a), shows the initial distribution and note that the slots are oriented in opposite directions for the two cylinders such that they are symmetric with respect to the flow. The second initial condition we considered is a quasi-smooth twin cosine-bell given by

$$U^{(cb)}(\lambda,\theta,t=0)=\begin{cases} b+ch_1(\lambda,\theta) & \text{if} \quad r_1<r, \\ b+ch_2(\lambda,\theta) & \text{if} \quad r_2<r, \\ b & \text{otherwise,} \end{cases} \tag{4.7}$$

where $c=0.9$, $b=0.1$ again is the background value, and

$$h_i(\lambda,\theta)=\frac{1}{2}[1+\cos(\pi r_i/r)] \quad \text{if} \quad r_i<r, \quad \text{for} \quad i=1,2.$$

The initial distribution is plotted in Figure 4.4(b). Note that this test is a variant of the slotted-cylinder case and we set all other parameters the same. The last one is a 'correlated' cosine-bell defined as

$$U^{(ccb)}(\lambda,\theta,t=0)=\psi(U^{(cb)}), \tag{4.8}$$

where ψ is non-linear quadratic function given by

$$\psi(\chi)=a_\psi\chi^2+b_\psi, \tag{4.9}$$

with $a_\psi=-0.8$ and $b_\psi=0.9$. This test is suggested by Lauritzen et al. in [17, 16] to assess the ability of a transport scheme to maintain pre-existing relations between species/tracers. The contour plot of the correlated cosine-bell is shown in Figure 4.4(c). Following [3], such pre-existing relations can be proved for the DG transport scheme.

First, we summarize the numerical results, including the normalized l_1, l_2, and l_∞ errors, for the discontinuous slotted-cylinder (4.6) and quasi-smooth twin cosine-bell (4.7) test cases in Table 4.1. The DG P^2 and P^3 schemes coupled with the simple WENO limiter and the BP filter are used for the simulations. Two sets of cubed-sphere meshes is adopted in order to compare the schemes with others reported in the literature. One is set as $30\times30\times6$ and $20\times20\times6$ for P^2 and P^3, respectively, corresponding to a $1.5°$ mesh resolution at the equator; the other is set as $60\times60\times6$ and $40\times40\times6$ for P^2 and P^3, respectively, corresponding to a $0.75°$ equatorial mesh resolution. We choose the time step to be $\Delta t=T/2000$ for the mesh with a $1.5°$ resolution and $\Delta t=T/4000$ for the mesh with a $0.75°$ resolution.

We first compare with the result obtained by the SEM with an optimization-based limiter reported in [10]. The motivation of the optimization limiter is similar to the BP filter in the sense that the maximum principle of schemes is enforced by locally adjusting the solution polynomial. However, it requires solving a quadratic program subject to linear constraints, and hence introduces more computational cost than the BP filter. In [10] Table 1 and Table 2, l_1, l_2, and l_∞ errors by SEMs P^3

DOI: 10.1002/fld

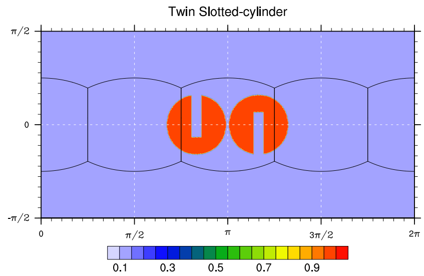

(a)

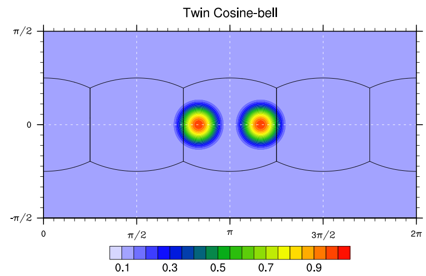

(b)

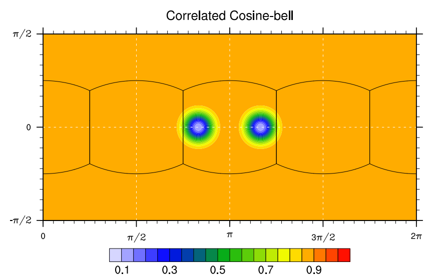

(c)

Figure 4.4. Three initial conditions for the deformational flow test. (a): Non-smooth twin slotted-cylinder. (b): Quasi-smooth twin cosine-bell. (c): 'Correlated' cosine-bell.

solving the same problem with a $1.5°$ resolution cubed-sphere mesh and a $0.75°$ one are reported, respectively. The errors by the DG P^3 with the WENO limiter and the BP filter are presented in Table 4.1. Those errors are slightly smaller than those by the SEMs with the optimization-based limiter (OP1). Moreover, for the twin cosine-bell case (4.7), the order of convergence in l_∞ errors degrades to first order accuracy from the SEM P^3 + OP1, while the second order accuracy is still maintained by the DG P^3 + WENO + BP. Note that the twin cosine-bell is C^1 smooth, thus the second order convergence is optimal we can expect.

We also compare the results with the DG schemes coupled with a H-WENO limiter and the BP filter presented in [35]. For a fair comparison, we set the configuration the same for the two schemes: a DG P^2 scheme is used on a cubed-sphere mesh $45 \times 45 \times 6$. The l_1, l_2, and l_∞ errors by from the DG P^2 + WENO + BP are 2.51E-2, 5.77E-2, and 1.38E-1, which are about 5% larger than those from the DG P^2 + H-WENO + BP in magnitude. However, we would like to remark again that the H-WENO limiter used in [35] only works for DG P^2, while the simple WENO limiter can be designed for DG schemes with arbitrarily high-order polynomial spaces.

Figure 4.5 shows the results for the case with the twin slotted-cylinder as the initial conditions. Note that the tracer is stretched into thin filaments following the highly deformational flow at time

DOI: 10.1002/fld

Table 4.1. Summary for results by the DG P^2 and P^3 schemes for the deformational flow test. The simple WENO limiter and the BP filter are coupled into the DG transport. Two sets of cubed-sphere meshes are used, which correspond to a equatorial $1.5°$ resolution and a equatorial $0.75°$ resolution, respectively. The normalized l_1, l_2, and l_∞ errors are reported at $T = 5$ for comparison.

Scheme	Tracer	Resolution	Time step	l_1	l_2	l_∞
P^2 + WENO + BP	Cos.	$1.5°$	$T/2000$	6.63E-2	1.44E-2	2.78E-1
P^2 + WENO + BP	Cyl.	$1.5°$	$T/2000$	2.60E-1	3.28E-1	7.01E-1
P^3 + WENO + BP	Cos.	$1.5°$	$T/2000$	3.15E-2	5.83E-2	1.20E-1
P^3 + WENO + BP	Cyl.	$1.5°$	$T/2000$	2.34E-1	2.94E-1	6.39E-1
P^2 + WENO + BP	Cos.	$0.75°$	$T/4000$	1.07E-2	2.55E-2	6.85E-2
P^2 + WENO + BP	Cyl.	$0.75°$	$T/4000$	1.62E-1	2.41E-1	6.52E-1
P^3 + WENO + BP	Cos.	$0.75°$	$T/4000$	8.43E-3	2.22E-2	8.32E-2
P^3 + WENO + BP	Cyl.	$0.75°$	$T/4000$	1.45E-1	2.20E-1	6.18E-1

$t = T/2$ and comes back to its initial state at $t = T$ as the flow reverses. The numerical results are comparable to those by other transport schemes reported in the literature, such as the non-oscillatory DG P^2 scheme with a H-WENO limiter and the BP filter in [35] and the SEMs with the optimization-based limiter [10].

At last, we investigate the ability of correlation preservation for the proposed schemes. Such a diagnostic is suggested by Lauritzen et al. in [17] and [16] to assess the ability of a transport scheme in preserving a pre-existing nonlinear relations between two tracers. In the test, the twin cosine-bell (4.7) and the correlated cosine-bell (4.8) are advected by the proposed schemes along the deformational flow. In the simulation, we use cubed-sphere meshes with $0.75°$ equatorial resolutions for both DG P^2 and P^3 schemes. In Figure 4.6, we report the scatter plots of the two non-linear correlated tracers at $t = T/2$, in which three numerical mixing diagnostics: 'real' mixing l_r, 'range-preserving' unmixing l_u, and overshooting l_o based on the scatter plots are also included. The definitions of l_r, l_u, and l_o are given in [16]. It is observed that the standard DG schemes can preserve the pre-existing quadratic relation between the two tracers very well. However, the overshooting error l_o is non-zero, which means the numerical unmixing is out of the range of the initial data. It is unacceptable when positivity preservation is required. On the other hand, the proposed schemes can effectively keep the solutions within the initial bound, and hence l_o equals to zero. But l_r, l_u are observed to be slighter larger than those by the standard DG schemes.

5. CONCLUDING REMARKS

In this paper, an efficient WENO (Weighted Essentially Non-Oscillatory) limier is proposed for the discontinuous Galerkin (DG) transport schemes on the cubed sphere. It is well known that DG schemes may produce unphysical oscillations when the solution is not smooth. Usually, a limiting strategy is imperative to suppress the undesirable oscillations and enhance the numerical stability. There are several requirements that a good limiter should fulfill. For instance, it should be robust to control oscillations, high-order accurate, and easy to implement. The situation is similar when the DG schemes are applied to the global transport simulations on a cubed-sphere mesh. However, the development of efficient limiters is even more challenging due to the inherent complication of the cubed-sphere geometry. In order to address the issue, we extended a simple WENO limiter on the Cartesian mesh to the cubed-sphere geometry. The limiter is local, uses information only from immediate neighbors, which results in a very compact stencil. Moreover, both uniform high-order accuracy and non-oscillatory property are obtained. When coupling the simple WENO limiter in the DG schemes on the cubed sphere, a special attention should be given at the cubed edges, where the curvilinear coordinates are discontinuous. We developed a boundary treatment to circumvent the difficulty, and high-order accuracy is retained. Another attractive of the simple WENO limiter

DOI: 10.1002/fld

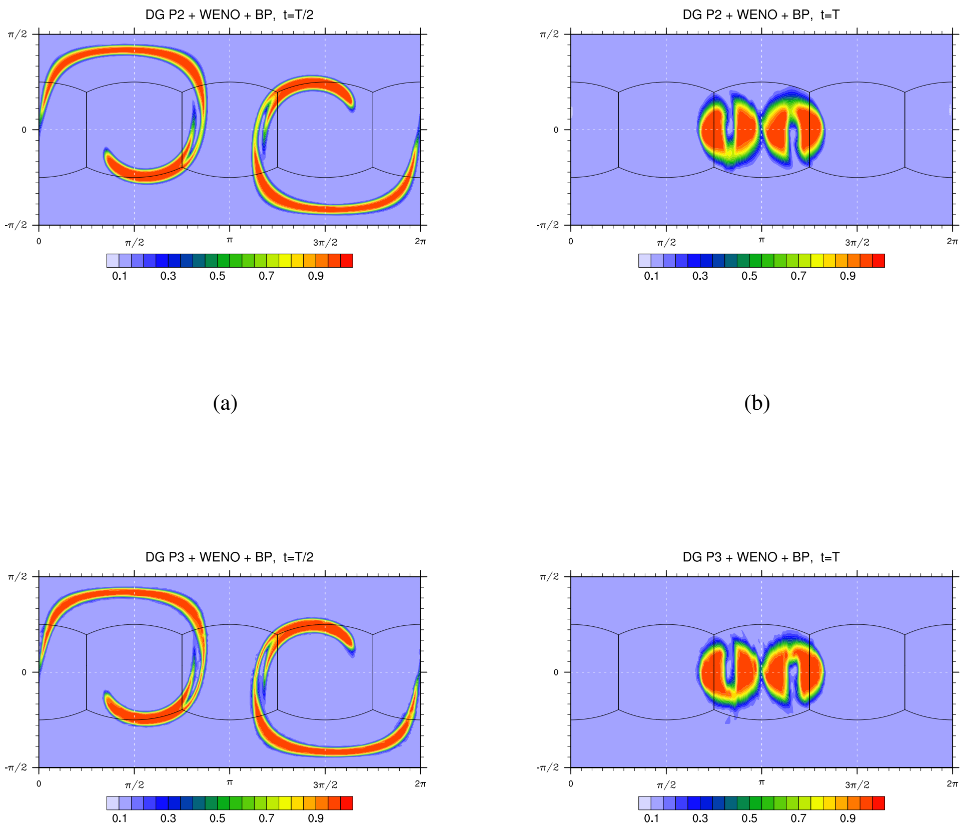

(a) (b)

(c) (d)

Figure 4.5. Numerical solutions for the deformational flow test with twin slotted-cylinder as the initial condition. The DG P^2 and P^3 schemes with the WENO limiter and the BP filter are applied on cubed-sphere meshes with a equatorial 0.75° resolution. The time step is set as $\Delta t = T/4000$. (a) The numerical solution by DG P^2 at half time $t = T/2$; (b) the numerical solution by DG P^2 at time $t = T$; (c) the numerical solution by DG P^3 at half time $t = T$; (d) the numerical solution by DG P^3 at half time $t = T$. Also note that, the numerical solution is exactly positivity preserving.

is that, unlike previous WENO limiters, it avoids ghost cells when applied to a corner cell of the cubed sphere, which leads to convenient implementation. Extensive numerical results for several benchmark spherical transport problems including solid-body rotation and deformational flow are provided to demonstrate good results, both in accuracy and in non-oscillatory performance. Future work consists of applying the efficient WENO limiter to the shallow-water model on the sphere.

ACKNOWLEDGMENTS

WG is supported by Research and Supercomputing Visitor Program (RSVP) in the Computational and Information Systems Laboratory (CISL) at the National Center for Atmospheric Research

DOI: 10.1002/fld

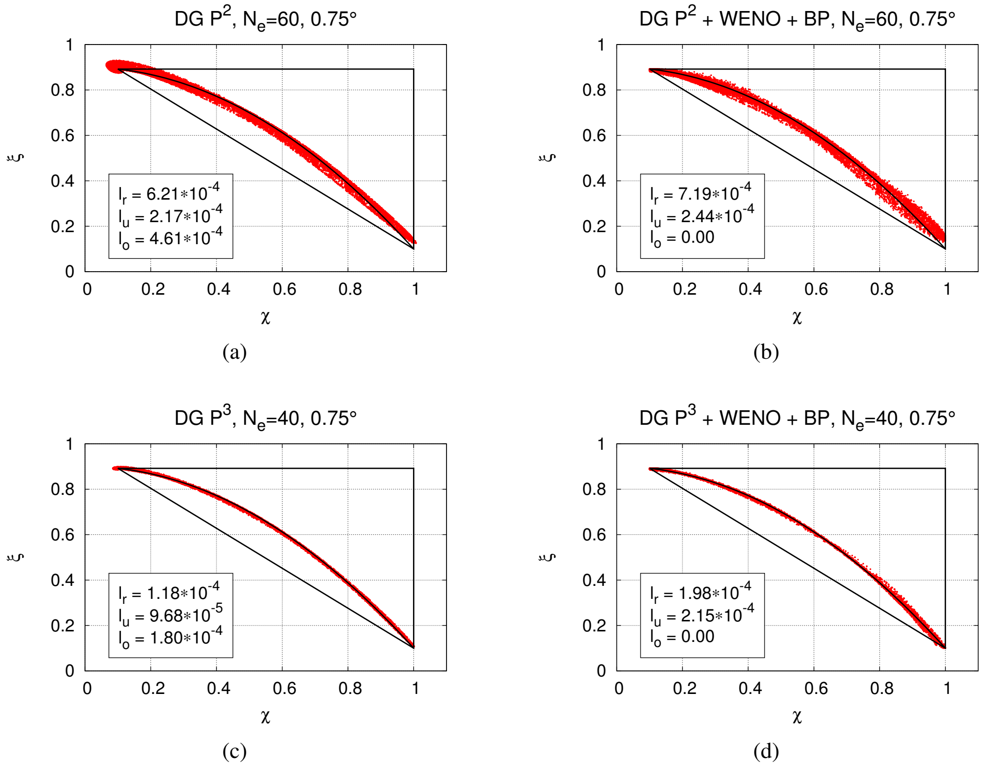

Figure 4.6. Scatter plots at $t = T/2$ for two non-linearly correlated tracers based on the twin cosine-bell (4.7) initial conditions. The mesh resolution is set as 0.75° in the simulations. (a) The standard DG P^2 scheme; (b) the DG P^2 + WENO + BP scheme; (c) the standard DG P^3 scheme; (d) the DG P^3 + WENO + BP scheme. The mixing diagnostics l_r, l_u, and l_o for correlation preservation are presented in each plot.

(NCAR). The support from CISL and NCAR is greatly appreciated. We would like to thank Prof. Chi-Wang Shu for many helpful discussions and suggestions. RDN would like to thank Dr. P. Lauritzen for an internal review. XZ would like to sincerely thank Dr. Yingda Cheng for her support. We gratefully acknowledge the support from the Michigan Center for Industrial and Applied Mathematics and Department of Mathematics of Michigan State University.

REFERENCES

1. D. Balsara and C.-W. Shu. Monotonicity preserving weighted essentially non-oscillatory schemes with increasingly high order of accuracy. *Journal of Computational Physics*, 160:405–452, 2000.
2. L. Bao, R. D. Nair, and H. M. Tufo. A mass and momentum flux-form high-order Discontinuous Galerkin shallow water model on the cubed-sphere. *J. Comput. Phys.*, 271:224–243, 2014.
3. P. Blossey and D. Durran. Selective monotonicity preservation in scalar advection. *J. Comput. Phys.*, 227(10):5160–5183, 2008.
4. B. Cockburn, S. Hou, and C.-W. Shu. The Runge-Kutta local projection discontinuous Galerkin finite element method for conservation laws IV: The multidimensional case. *Math. Comput.*, 54:545–581, 1990.
5. B. Cockburn and C.-W. Shu. Runge–Kutta discontinuous Galerkin methods for convection-dominated problems. *J. Sci. Comput.*, 16(3):173–261, 2001.
6. J. Dennis, M. Taylor, M. Levy, and Co-authors. CAM-SE: A scalable spectral-element dynamical core for the Community Atmosphere Model. *Int. J. High. Perform. C*, 26:74–89, 2011.
7. M. Dumbser and M. Käser. Arbitrary high order non-oscillatory finite volume schemes on unstructured meshes for linear hyperbolic systems. *Journal of Computational Physics*, 221:693–723, 2007.
8. F. Giraldo, J. Hesthaven, and T. Warburton. Nodal high-order Discontinuous Galerkin methods for spherical shallow water equations. *J. Comput. Phys.*, 181:499–525, 2002.

9. S. Gottlieb, D. Ketcheson, and C.-W. Shu. High order strong stability preserving time discretizations. *Journal of Scientific Computing*, 38(3):251–289, 2009.
10. O. Guba, M. Taylor, and A. St-Cyr. Optimization-based limiters for the spectral element method. *J. of Comput. Phys.*, 267:176–195, 2014.
11. W. Guo, R. Nair, and J.-M. Qiu. A conservative semi-Lagrangian discontinuous Galerkin scheme on the cubed-sphere. *Mon. Wea. Rev.*, 142(1):457–475, 2013.
12. D. Hall and R. Nair. Discontinuous Galerkin transport on the spherical Yin-Yang overset mesh. *Mon. Wea. Rev.*, 142:264–282, 2013.
13. C. Hu and C.-W. Shu. Weighted essentially non-oscillatory schemes on triangular meshes. *Journal of Computational Physics*, 150:97–127, 1999.
14. G. Jiang and C.-W. Shu. Efficient implementation of weighted ENO schemes. *Journal of Computational Physics*, 126:202–228, 1995.
15. M. Käser and A. Iske. ADER schemes on adaptive triangular meshes for scalar conservation laws. *Journal of Computational Physics*, 205:486–508, 2005.
16. P. Lauritzen, W. Skamarock, M. Prather, and M. Taylor. A standard test case suite for two-dimensional linear transport on the sphere. *Geosci. Model Dev.*, 5(3):887–901, 2012.
17. P. Lauritzen and J. Thuburn. Evaluating advection/transport schemes using interrelated tracers, scatter plots and numerical mixing diagnostics. *Q. J. Roy. Meteorol. Soc.*, 138(665):906–918, 2012.
18. M. N. Levy, R. D. Nair, and H. M. Tufo. High-order Galerkin method for scalable global atmospheric models. *Computers and Geoscience*, 33:1022–1035, 2007.
19. H. Luo, J. D. Baum, and R. Lohner. A Hermite WENO-based limiter for discontinuous Galerkin method on unstructured grids . *Journal of Computational Physics*, 225(1):686 – 713, 2007.
20. R. Nair and P. Lauritzen. A class of deformational flow test cases for linear transport problems on the sphere. *J. Comput. Phys.*, 229(23):8868–8887, 2010.
21. R. Nair, S. Thomas, and R. Loft. A discontinuous Galerkin transport scheme on the cubed sphere. *Mon. Wea. Rev.*, 133(4):814–828, 2005.
22. R. D. Nair, H.-W. Choi, and H. M. Tufo. Computational aspects of a scalable high-order discontinuous Galerkin atmospheric dynamical core. *Comput Fluids*, 38:309–319, 2009.
23. R. D. Nair, M. N. Levy, and P. H. Lauritzen. Emerging numerical methods for atmospheric modeling. In P. H. Lauritzen, C. Jablonowski, M. A. Taylor, and R. D. Nair, editors, *Numerical Techniques for Global Atmospheric Models*, volume 80, pages 189–250. Springer-Verlag, 2011. LNCSE.
24. J. Qiu and C.-W. Shu. Hermite WENO schemes and their application as limiters for Runge–Kutta discontinuous Galerkin method: one-dimensional case. *J. Comput. Phys.*, 193(1):115–135, 2004.
25. J. Qiu and C.-W. Shu. A comparison of troubled-cell indicators for Runge–Kutta discontinuous Galerkin methods using weighted essentially nonoscillatory limiters. *SIAM J. Sci. Comput.*, 27(3):995–1013, 2005.
26. J. Qiu and C.-W. Shu. Hermite WENO schemes and their application as limiters for Runge-Kutta discontinuous Galerkin method II: Two dimensional case. *Computers and Fluids*, 34(6):642 – 663, 2005.
27. J. Qiu and C.-W. Shu. Runge-Kutta discontinuous Galerkin method using WENO limiters. *SIAM J. Sci. Comput.*, 26(3):907–929, 2005.
28. W. Reed and T. Hill. Triangular mesh methods for the neutron transport equation. Technical Report LA-UR-73-479, Los Alamos Scientic Laboratory, Los Alamos, 1973.
29. C. Ronchi, R. Iacono, and P. Paolucci. The cubed sphere: a new method for the solution of partial differential equations in spherical geometry. *J. Comput. Phys.*, 124(1):93–114, 1996.
30. R. Sadourny. Conservative finite-difference approximations of the primitive equations on quasi-uniform spherical grids. *Mon. Wea. Rev.*, 100(2):136–144, 1972.
31. C.-W. Shu. Essentially non-oscillatory and weighted essentially non-oscillatory schemes for hyperbolic conservation laws. Technical Report NASA CR-97-206253 ICASE Report No. 97-65, Institute for Computer Applications in Science and Engineering (ICASE), 1997.
32. C.-W. Shu and S. Osher. Efficient implementation of essentially non-oscillatory shock-capturing schemes. *Journal of Computational Physics*, 77:439–471, 1988.
33. D. Williamson, J. Drake, J. Hack, R. Jakob, and P. Swarztrauber. A standard test set for numerical approximations to the shallow water equations in spherical geometry. *J. Comput. Phys.*, 102(1):211–224, 1992.
34. X. Zhang and C.-W. Shu. On maximum-principle-satisfying high order schemes for scalar conservation laws. *Journal of Computational Physics*, 229(9):3091 – 3120, 2010.
35. Y. Zhang and R. Nair. A Nonoscillatory discontinuous Galerkin transport scheme on the cubed-sphere. *Mon. Wea. Rev.*, 140:3106–3126, 2012.
36. X. Zhong and C.-W. Shu. A simple weighted essentially nonoscillatory limiter for Runge-Kutta discontinuous Galerkin methods. *Journal of Computational Physics*, 232(1):397–415, 2013.
37. J. Zhu, X. Zhong, C.-W. Shu, and J. Qiu. Runge-Kutta discontinuous Galerkin method using a new type of WENO limiters on unstructured meshes. *Journal of Computational Physics*, 248:200–220, 2013.

DOI: 10.1002/fld